



Marigold-flower-like $\text{TiO}_2/\text{MIL-125}$ core–shell composite for enhanced photocatalytic Cr(VI) reduction

Yu-Xuan Li, Chong-Chen Wang^{*}, Huifen Fu, Peng Wang

Beijing Key Laboratory of Functional Materials for Building Structure and Environment Remediation/Sino-Dutch R&D Centre for Future Wastewater Treatment Technologies, Beijing University of Civil Engineering and Architecture, Beijing 100044, China

ARTICLE INFO

Editor: Dr. Zhang Xiwang

Keywords:

MIL-125

TiO_2

Post-solvothermal treatment

Cr(VI) reduction

Photocatalysis

ABSTRACT

Series $\text{TiO}_2/\text{MIL-125}$ core-shell composites were fabricated from MIL-125 via in-situ post-solvothermal method. The composites composed of TiO_2 as shell and MIL-125 as core demonstrated some advantages like abundant linker defects, mesoporous structure and unsaturated titanium-oxo clusters, which enabled it to be a desired photocatalyst. The photocatalytic Cr(VI) reduction performances of as-prepared $\text{TiO}_2/\text{MIL-125}$ composites with different treatment times were evaluated under Xe lamp irradiation. The results indicated that optimal marigold-flower-like MT-2 ($\text{TiO}_2/\text{MIL-125}$ composite produced by treating MIL-125 for 2 h) exhibited superior photocatalytic Cr(VI) reduction activity than those of pristine MIL-125 precursor, $\text{TiO}_2/\text{MIL-125}$ composites produced by treating MIL-125 for 1 h, and the completely derived TiO_2 . The TiO_2 nanosheet formed from the outer-to-inner loss of organic ligands in the MIL-125 precursor can boost the separation efficiency of photo-induced carriers. Within this work, the influence of operation factors including pH values, foreign ions and organic acids with small molecular weight on photocatalytic Cr(VI) reduction were explored. The apparent quantum efficiency of optimal MT-2 was calculated under different monochromatic light. As well, the possible mechanism of photocatalytic Cr(VI) reduction over MT-2 was proposed and confirmed by electrochemical determination, active species trapping experiments and electron spin resonance analyses.

1. Introduction

Photocatalysis can utilize the endless, clean and safe energy of the sun to achieve sustainable, harmless and economically feasible technology [1]. Researchers have been devoting to develop some efficient photocatalysts. Recently, metal organic frameworks (MOFs), constructed from metal ions as templates coordinated by organic linkers, have received widespread attention as the alternative photocatalysts, due to their advantages of versatile structures, various functionalities, abundant active sites and large specific surface area [2,3]. As one of the classic MOFs photocatalyst, MIL-125 possesses the excellent properties such as high density of Ti sites, good encapsulation capability and high porosity [4,5]. However, the applications of MIL-125(Ti) are limited because of the low photocatalytic activity resulted from the wide band gap, the rapid electron-hole recombination and instability [6]. In order to improve the performances of MOFs, various strategies are proposed, including but not limited introducing extra components like metals and/or semiconductors as well as obtaining derivatives of MOF precursors [7–10]. For example, Yuan and coworkers synthesized

$\text{Ag/rGO/MIL-125(Ti)}$ ternary heterojunction to achieve RhB photodegradation under visible light [6]. Yuan and coworkers also fabricated $\text{In}_2\text{S}_3/\text{MIL-125(Ti)}$ microparticle photocatalyst to eliminate tetracycline from wastewater [11]. Yang and coworkers constructed MIL-125/ $\text{Ag/g-C}_3\text{N}_4$ for nitrobenzene reduction and alcohols oxidation upon the irradiation of visible light [12]. Wang and coworkers prepared disk-like N- TiO_2 by calcining the matrix of MIL-125(Ti) and melamine to realize photocatalytic benzene degradation [13]. Zhang and coworkers fabricated TiO_2/C derived from MIL-125(Ti) for photocatalytic tetracycline degradation [14].

Currently, employing MOFs as precursors to obtain the derivatives is considered to be one of the effective ways to obtain the active and effective photocatalysts [15], which could be attributed to the following reasons. Firstly, the specific topologies, morphologies and structures of MOFs can be maintained in their derivatives. Secondly, agglomeration of active sites and collapse of structure could be avoided. Therefore, MOF-derived materials can retain the advantages of their precursors including adjustable pore size, porosity and flexible designability [16, 17]. It is worth noting that the utilization of post-solvothermal method

^{*} Corresponding author.

E-mail addresses: wangchongchen@bucea.edu.cn, chongchenwang@126.com (C.-C. Wang).

<https://doi.org/10.1016/j.jece.2021.105451>

Received 3 February 2021; Received in revised form 27 March 2021; Accepted 4 April 2021

Available online 12 April 2021

2213-3437/© 2021 Elsevier Ltd. All rights reserved.

to prepare heterojunction for photocatalysis has achieved satisfactory results. Series composites like $\text{In}_2\text{S}_3/\text{NH}_2\text{-MIL-68(In)@In}_2\text{S}_3$ sandwich homologous heterojunction as well as $\text{MIL-125-NH}_2/\text{TiO}_2$ core-shell particles have accomplished efficient photocatalytic CO_2 reduction and H_2 production [18,19]. At present, the fabrication of identical heterojunctions derived from MOFs for water purification are tapping a new door.

Hexavalent chromium (Cr(VI)) has been one of the typical heavy metal pollutants in wastewater, especially in the polluted water discharged from electroplating, leather, metallurgy and so on [7]. Cr(VI) is mainly in the forms of HCrO_4^- or CrO_4^{2-} , which exhibited strong toxicity to aquatic organisms and human organs due to the water solubility and carcinogenicity [20]. Compared with high-toxic Cr(VI) , trivalent chromium (Cr(III)) displays low toxicity, which could easily form Cr(OH)_3 precipitates under alkaline or neutral conditions. Photocatalytic Cr(VI) reduction into Cr(III) has been extensively studied and is considered to be one of the effective and low-cost methods [21,22].

Within this study, $\text{TiO}_2/\text{MIL-125}$ composites were fabricated via the in-situ post-solvothermal treatment toward MIL-125 in the presence of thioacetamide (TAA), in which the marigold-flower-like $\text{TiO}_2/\text{MIL-125}$ core-shell composite (MT-2) exhibited superior photocatalytic Cr(VI) performances upon the 300 W Xe lamp with ultraviolet reflector. The marigold-flower-like MT-2 displayed good stability and reusability. Finally, the photocatalytic Cr(VI) reduction mechanism was proposed and verified.

2. Experimental

2.1. Materials and instruments

The used materials, the instruments and the corresponding methods were listed in electronic [Supplementary Information](#) (ESI).

2.2. Synthesis of MIL-125

Disk-like MIL-125(Ti) was synthesized according to the previous method [23,24]. In detail, 2.2 g of 1,4-benzenedicarboxylic acid (BDC) was dissolved in 36 mL N,N -dimethylformamide (DMF) with the aid of ultrasonication. Then, 4.0 mL methanol and 2.4 mL tetrabutyl titanate are sequentially mixed with the above solution. The matrix was transferred into Teflon-lined stainless-steel autoclave and heated at 150°C for 48 h. The obtained materials were washed twice by DMF and dried at 80°C in a vacuum oven.

2.3. Synthesis of $\text{TiO}_2/\text{MIL-125}$ composites

The $\text{TiO}_2/\text{MIL-125}$ core-shell composites were fabricated by solvothermal method. In particular, 0.1 g of as-synthesized MIL-125(Ti) and 0.4 g of thioacetamide (TAA) were put into the ethanolic solution. The above solution was sealed in the Teflon-lined stainless-steel autoclave and heated for 1 h, 2 h, 3 h, 6 h at 180°C to acquire MT-1, MT-2, MT-3 and MT-6, respectively. The obtained products were washed three times by ethanol and dried in an oven at 60°C (Scheme 1).

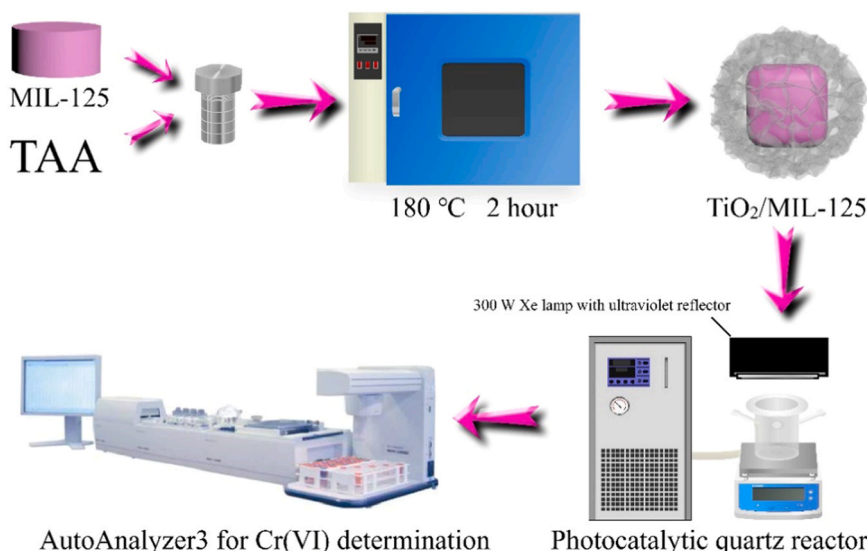
2.4. Photocatalytic activity test

Photocatalytic Cr(VI) reduction experiments were performed in a quartz reactor containing the suspension of 15.0 mg as-prepared photocatalyst and 50.0 mL Cr(VI) aqueous solution. The pH values of the reaction system were regulated to 2.0–8.0 by adding H_2SO_4 or NaOH solutions. Firstly, the mixture was stirred to achieve the absorption-desorption equilibrium in dark. Then, the suspensions were irradiated under 300 W Xe lamp with ultraviolet reflector (Beijing Aulight Co. Ltd) (the light spectrum of the light is found in Fig. S1). The 1.5 mL aliquots were taken out and filtered by $0.22\ \mu\text{m}$ PTFE membrane every 10.0 min to determine the residual Cr(VI) concentrations via diphenylcarbazide (DPC) method on AutoAnalyzer 3 Flow Injection Analyzer (Seal Analytical Co. Ltd). The continuous flow analysis method displays some advantages like low reagent consumption, high accuracy as well as high precision [25,26].

The apparent quantum efficiencies (AQE) were measured under different wavelengths of light provided by a 300 W Xe lamp with different light filters, which was obtained via calculating the amount of removed pollutant. The equation of AQE for photocatalytic Cr(VI) reduction and incident photons followed Eqs. (1) and (2), respectively [27,28].

$$\text{AQE}(\text{Cr}) = \frac{3 \times [\text{number of reduced Cr(VI)}]}{\text{number of incident photons}} \quad (1)$$

$$N_p^i = \frac{P\lambda}{hc} \quad (2)$$



Scheme 1. Synthetic illustration for the preparation of $\text{TiO}_2/\text{MIL-125}$ composites and photocatalytic Cr(VI) degradation process.

3. Results and discussion

3.1. Material characterizations

The powder X-ray diffraction (PXRD) patterns of the as-synthesized MIL-125 matched perfectly with both the simulated patterns from the single crystal data (CCDC 751157) and those reported in previous literatures [29], indicating that the pure MIL-125 was obtained successfully (Fig. S2). The MIL-125 was etched by TAA for 1 h, 2 h, 3 h and 6 h via solvothermal method to produce MT-1, MT-2, MT-3 and MT-6, respectively. The PXRD patterns of MT-1 and MT-2 revealed that the major characteristic peaks of MIL-125 at 6.8° , 9.7° , 11.7° , 15.2° and 16.8° could be obviously observed, demonstrating the presence of partial MIL-125. However, the disappearance of typical peaks of MIL-125 after being treated for 3 h and 6 h implied that MIL-125 was completely destructed. It could be noticed from Fig. 1a that new peaks at 25.7° , 48.7° and 62.9° were observed in MT-2, which was assigned to the (101), (200) and (204) lattice planes of anatase TiO_2 [30–32], indicating that the $\text{TiO}_2/\text{MIL-125}$ composites were fabricated. With the increasing etching time, the pure anatase TiO_2 was produced, and characteristic PXRD peaks of MT-3 and MT-6 matched well with JCPDS (PDF#01–070–6826).

In the FTIR spectra of MIL-125 (Fig. 1b), the characteristic bands in the range of $400\text{--}800\text{ cm}^{-1}$ were ascribed to Ti–O–Ti stretching vibrations. The bands at 1400 and 1657 cm^{-1} could be attributed to the vibrational stretching frequencies of O–C–O attached to the dicarboxylate linker. It could be observed that the peak at 1013 cm^{-1} corresponded to benzene rings vibrations [12,33]. However, in the FTIR spectra of the as-prepared composites, the typical peaks of MIL-125 became weaker with the prolonged treatment time. It was worth noting that all the characteristic peaks of MIL-125 were completely

disappeared in MT-6. The peak at 1630 cm^{-1} in MT-6 spectra could be assigned to O–H bending band. Especially, the bands at $400\text{--}800\text{ cm}^{-1}$, 1031 cm^{-1} and 1400 cm^{-1} were remained in the spectra of MT-2, further confirming the partial presence of MIL-125 in MT-2.

The successful fabrication of $\text{TiO}_2/\text{MIL-125}$ was further confirmed by thermal gravity analysis (TGA), in which the weight loss can provide some information of guest molecules and organic ligands composition (Fig. 5a). For the MIL-125, two steps weight loss can be observed. The first weight loss appeared in the range of $50\text{--}250^\circ\text{C}$, which was attributed to the removal of guest molecules like H_2O , methanol and DMF. The second weight loss occurred at ca. 400°C due to the decomposition of BDC linkers [29], which was affirmed by the obviously exothermic peak in the differential scanning calorimetry (DSC) plot. In the pristine MIL-125, the calculated weight loss (%) of BDC linkers were 32%. While as to the derivatives, the content of organic linkers decreased with the increasing etching time, which resulted into the reduced weight loss (23% for MT-1, 9% for MT-2). It worth noting that the weight loss of MT-6 was negligible even when it was treated at 400°C , confirming the complete loss of organic linker in MT-6.

It has been reported that core-shell structure could be formed by post-solvothermal [19,34]. As depicted in Fig. 2a, the pristine MIL-125 was smooth regular disc and the particle size ranged from 300 nm to 2400 nm . SEM images (Fig. 2b and c) showed that MT-1 and MT-2 well maintained the shape of disc, while MT-3 and MT-6 demonstrated hollow disc or unregular morphology and consisted of nanosheets (Fig. 2d and e). Especially, MT-2 presented the specific morphology of Inca marigold, in which the formed TiO_2 is just like outer petals. The formation mechanism of Inca marigold-like $\text{TiO}_2/\text{MIL-125}$ could be described as: the disc-like MIL-125 was internally and externally etched to achieve BDC linker loss in the process of solvothermal method, leading to the generation of core-shell structure [35,36].

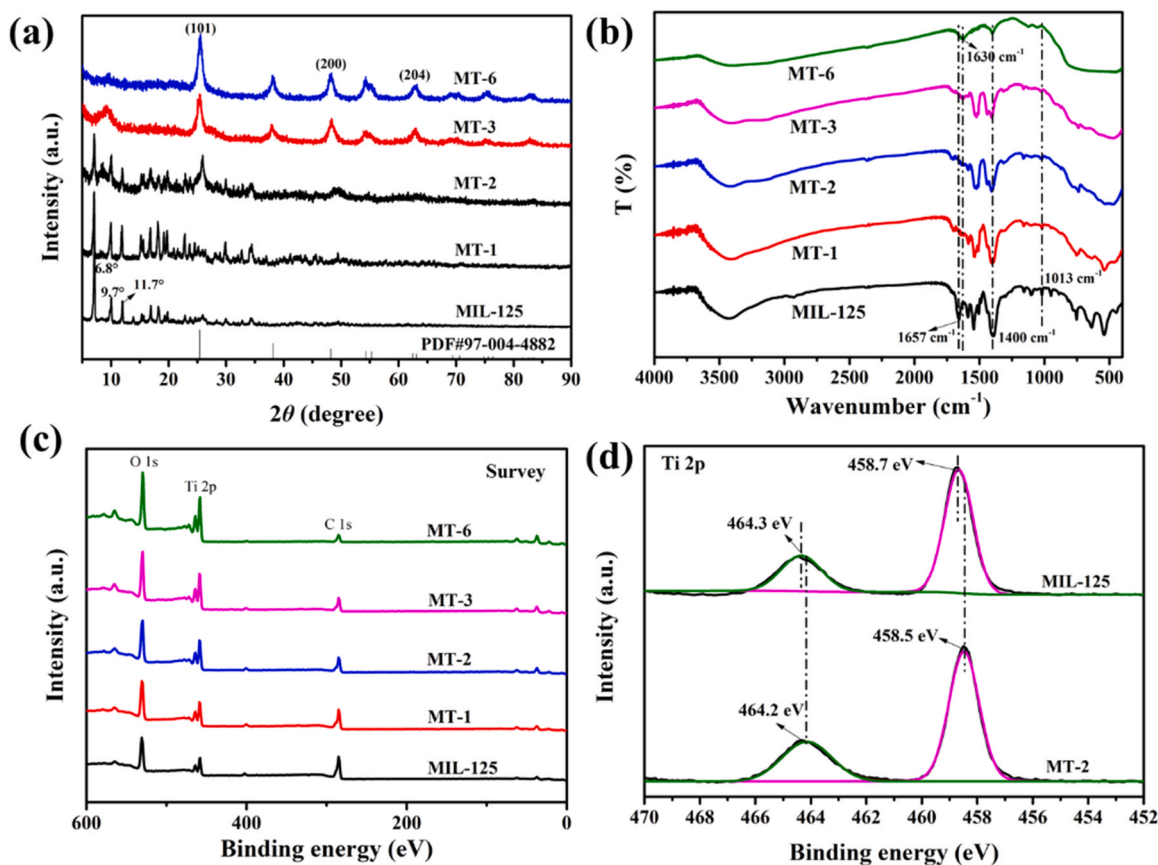


Fig. 1. (a) PXRD patterns (note: PDF#97–004–4882: PDF standard card of anatase TiO_2); (b) FT-IR spectra, and (c) XPS spectra of MIL-125 and MT-x; (d) the Ti 2p spectra in MIL-125 and MT-2.

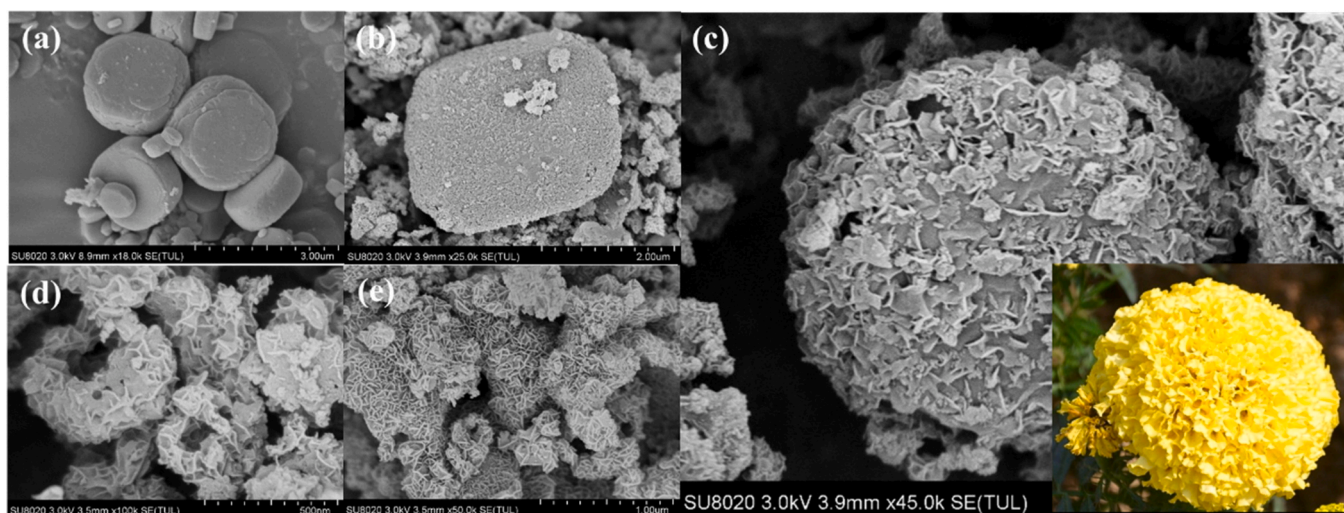


Fig. 2. SEM images of MIL-125 (a), MT-1 (b), MT-2 and Inca marigold (inset) (c), MT-3 (d) and MT-6 (e).

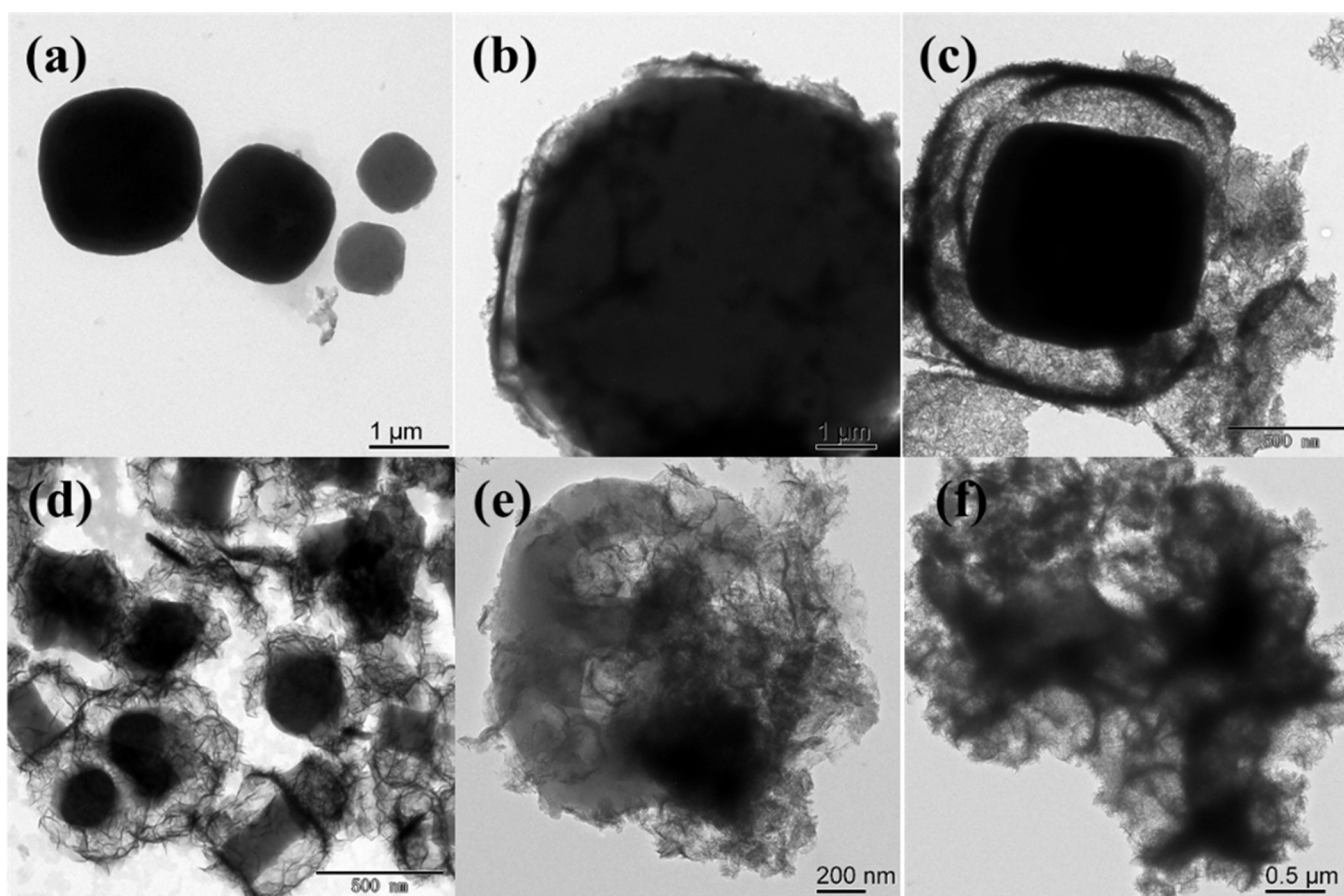


Fig. 3. TEM images of MIL-125 (a), MT-1 (b), MT-2 (c and d), MT-3 (e) and MT-6 (f).

From the observation of TEM images as illustrated in Fig. 3a and b, MT-1 displayed potential core-shell structure with thin shell. The TEM images of MT-2 demonstrated the obvious core-shell structure constructing from the formed TiO_2 as shell and the pristine MIL-125 as core, which were similar with MIL-125- NH_2 @ TiO_2 particles reported previously [19]. When the reaction time prolonged to 3 h, the morphology of the obtained products was hollow structure with the trend of becoming minor particles. As to MT-6, it was found that the structure was collapsed into TiO_2 sheets. To further prove that the outer shell of MT-2

was fabricated by TiO_2 derived from MIL-125, the HRTEM was applied to determine the lattice structure (Fig. 4b), in which the calculated lattice spacing was 0.352 nm and 0.353 nm, corresponding to (101) lattice plane of anatase TiO_2 [37,38]. As well, the selected area electron diffractograms (SAED) pattern of outer TiO_2 shell of MT-2 was shown in Fig. 4c. The diffraction rings of 0.352 nm and 0.190 nm could be attributed to (101) and (200) lattice plane of anatase TiO_2 [27,39], which was consistent with the PXRD and HRTEM results.

To investigate the internal structure of TiO_2 /MIL-125, the XPS

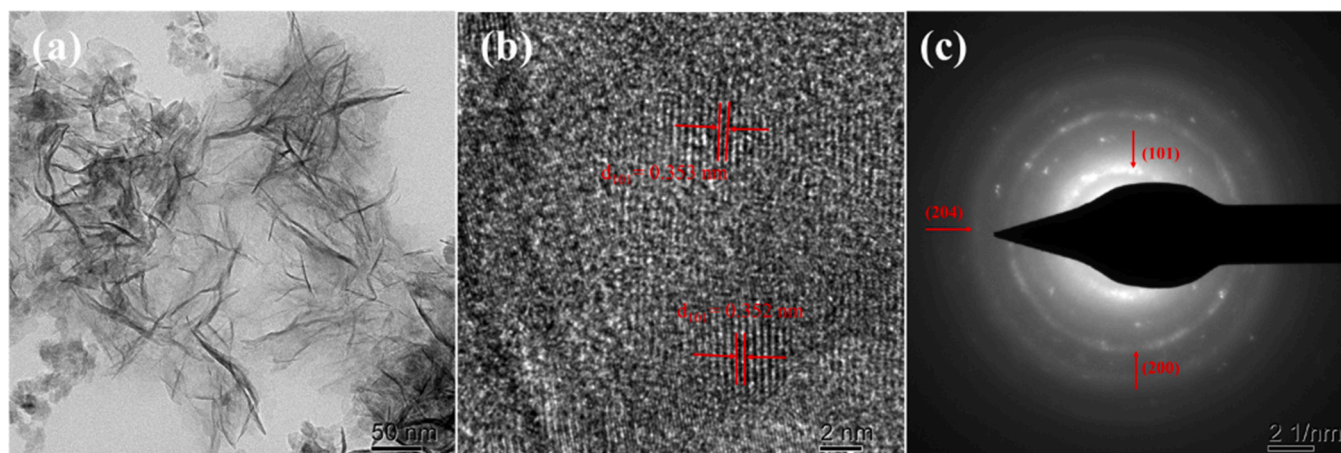


Fig. 4. TEM (a), HRTEM (b) and SAED (c) of TiO_2 shell in MT-2.

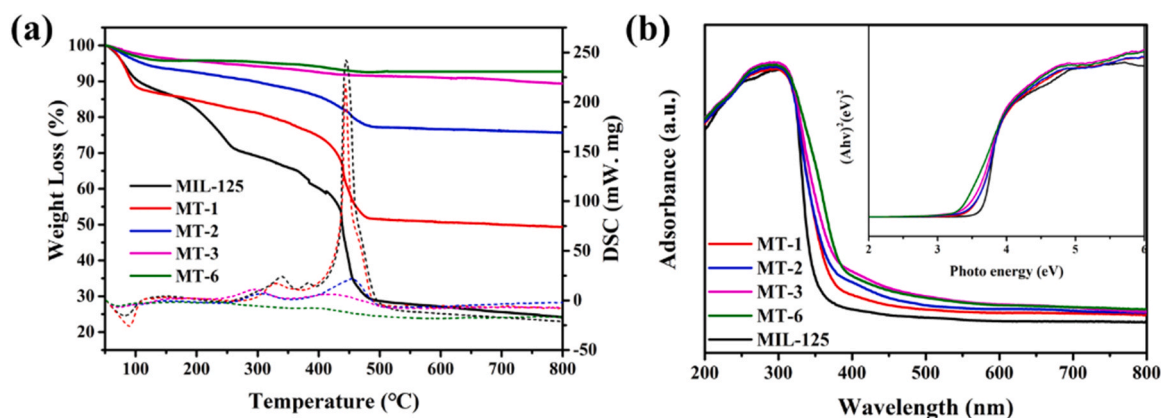


Fig. 5. TGA curves (a), UV-vis DRS and E_g plot (inset) of different photocatalysts (b).

determination was conducted. The XPS survey spectra suggested that MIL-125 and the derivatives both exhibited O 1s, Ti 2p and C 1s peaks (Fig. 1c). However, the peak intensity of C 1s weakened while the peak intensities of O 1s and Ti 2p became stronger with elongated treatment time. In Ti 2p spectrum (Fig. 1d), two peaks with binding energy at 458.7 eV and 464.3 eV in MIL-125 corresponded to Ti $2p_{3/2}$ and Ti $2p_{1/2}$ respectively, confirming the presence of Ti^{4+} in the titanium-oxo cluster. It worth noting that the peaks with binding energy at 458.7 eV and 464.3 eV of MIL-125 shifted to lower binding energy positions at 458.5 eV and 464.2 eV in MT-2, revealing the generation of Ti^{3+} and linker defects in MIL-125/ TiO_2 [34,40]. In O 1s XPS spectrum (Fig. S3), the characteristic peaks of MIL-125 at 529.6 eV and 531.4 eV could be attributed to lattice oxygen of titanium-oxo cluster and C-O in organic BDC linkers [41,42]. The binding energy of O 1s in MT-2 is higher than that of MIL-125, implying the electron transfer between Ti-O cluster.

The UV-vis DRS spectra exhibited the light adsorption properties of MIL-125 and the derivatives. As shown in Fig. 5b, the band gap (E_g) of pristine MIL-125 was estimated to be 3.66 eV. It was interesting to observe that the band gap decreased to 3.40 eV, 3.40 eV, 3.34 eV and 3.20 eV respectively for MT-1, MT-2, MT-3 and MT-6, indicating that the obtained composites could be excited by UV light with longer wavelength.

3.2. Photocatalytic Cr(VI) reduction activity

Since the TiO_2 shell composed of ultra-thin nanosheets could make the unsaturated titanium-oxo clusters highly exposed, further improving the light absorption performance as well as conductivity of

photocatalyst, the MT-2 might possess superior performances [19]. In this study, the Cr(VI) as the form of $\text{Cr}_2\text{O}_7^{2-}$ was selected as model pollutant to assess the photocatalytic reduction performances of MIL-125 and the obtained derivatives. As shown in Fig. 6a, the photocatalytic Cr(VI) reduction activities over MIL-125 and the derivatives under the Xe lamp irradiation were tested. After reaching the equilibrium of adsorption and desorption, it was found that neither MIL-125 nor the derivatives exhibited significant Cr(VI) adsorption performances. All the derivatives (MT-1, MT-2, MT-3 and MT-6) displayed better photocatalytic Cr(VI) reduction efficiencies than the pristine MIL-125. Especially, the optimal MT-2 with Inca marigold-flower-like TiO_2 /MIL-125 Core-Shell structure depicted superior photocatalytic Cr(VI) cleanup performance with 100.0% removal efficiency with 60 min to others derivatives like MT-3 (98.8% within 60 min), MT-6 (90.0% within 60 min) and MT-1 (64.5% within 60 min). The apparent reaction rate constants (k) calculated by the pseudo-first order model ($\ln[C/C_0] = -kt$) followed the order of MT-2 > MT-3 > MT-6 > MT-1 > MIL-125 (Fig. 6b), displaying noticeable saddle-shaped curve with MT-2's value at the top. Some cases of photocatalytic Cr(VI) reduction activities over some counterpart photocatalysts were selected to make objective comparison (Table 1) to evaluate the position of the optimal MT-2. From Table 1, it can be found the optimal MT-2 demonstrated best Cr(VI) cleanup performance among all the MIL-125-based photocatalysts.

The apparent quantum efficiencies (AQEs) of MT-2 toward Cr(VI) reduction at different wavelengths were calculated (Fig. 6c), which could be one of the criteria to evaluated photocatalytic performances [47]. The AQEs over MT-2 were 0.580% at 315 nm, 0.280% at 365 nm,

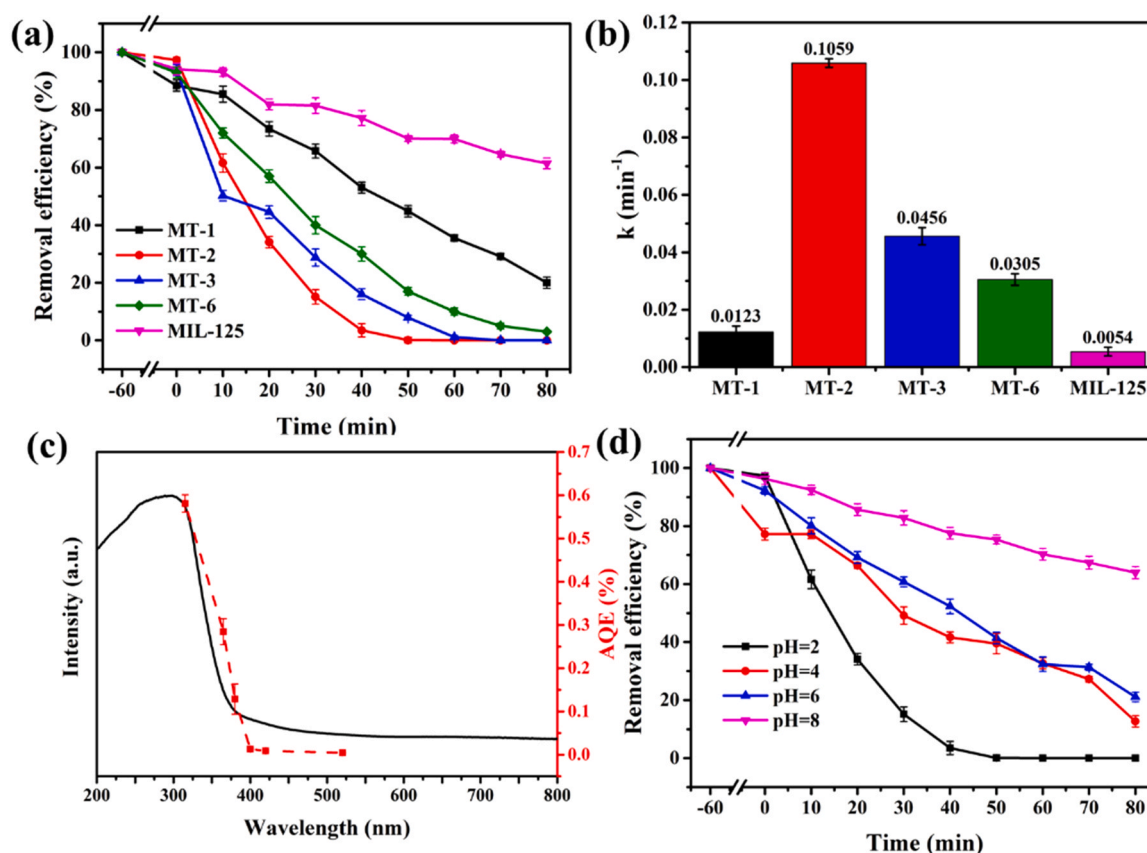


Fig. 6. Photocatalytic Cr(VI) reduction (a) and comparison of rate constant k (b) over MIL-125 and MT- x . AQE results of Cr(VI) reduction under different monochromatic light corresponding to the absorption spectrum (c). Influence of pH values on photocatalytic Cr(VI) reduction (d). Conditions: 15.0 mg (300 mg L⁻¹) of MT-2, Cr(VI) = 5.0 mg L⁻¹, 50 mL, pH = 2.0.

Table 1

Comparison of photocatalytic Cr(VI) removal activities of various MIL-125-based photocatalysts.

Catalyst/dosage (mg L ⁻¹)	Pollutants/mg L ⁻¹	Irradiation	pH	Efficiency (%)	k (min ⁻¹)	Ref
MIL-125-NH ₂ /1000	Cr(VI)/15	300 W Xe lamp	6	45.0% 120 min	–	[43]
Pt/MIL-125-NH ₂ /1000	Cr(VI)/15	300 W Xe lamp	6	75.0% 120 min	–	[43]
CuS/MIL-125(Ti)/500	Cr(VI)/48	300 W Xe lamp (420 nm filter)	6	53.0% 70 min	–	[44]
MoS ₂ /MIL-125(Ti)/500	Cr(VI)/48	300 W Xe lamp (420 nm filter)	6	33.3% 70 min	0.0060	[44]
CdS/MIL-125(Ti)/500	Cr(VI)/48	300 W Xe lamp (420 nm filter)	6	35.0% 70 min	0.0058	[44]
Ag ₂ S/MIL-125(Ti)/500	Cr(VI)/48	300 W Xe lamp (420 nm filter)	6	23.0% 70 min	0.0035	[44]
Bi ₂ S ₃ @NH ₂ -MIL-125(Ti)/100	Cr(VI)/10	300 W Xe lamp	7	77.0% 120 min	0.01134	[45]
Ag/Ag ₃ PO ₄ /MIL-125-NH ₂ /250	Cr(VI)/10	Visible light	2	100.0% 70 min	0.0621	[24]
MIL-125-derived TiO ₂ @C/300	Cr(VI)/5	–	3	61.8% 90 min	–	[46]
Marigold-flower-like MT-2/300	Cr(VI)/5	300 W Xe lamp	2	100.0% 60 min	0.1059	This work

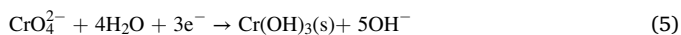
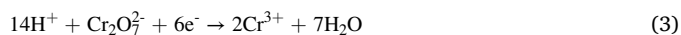
0.130% at 380 nm, 0.010% at 420 nm and 0.005% at 520 nm, respectively. It was worth noting that AQE values perfectly conformed to the trend of MT-2's UV-vis absorption spectrum, demonstrating the process of Cr(VI) reduction resulted from photocatalysis [48].

The BET specific surface area and N₂ adsorption-desorption isotherm results were shown in Table. S1 and Fig. S4. It can be observed that the pristine MIL-125 exhibited largest surface area and the increasing treating time could lead to decreasing surface areas from 514.00 m² g⁻¹ to 262.78 m² g⁻¹. Specifically, the specific surface area of MIL-125/TiO₂ composite was 345.66 m² g⁻¹, which corresponded to ligand loss in the process of solvothermal method and conversion from microporous structure to mesoporous structure. Previous literatures have reported that larger surface area might facilitate photocatalytic activities by exposing more active sites [49,50]. However, the mesoporous structure could facilitate the access of contaminants and appropriate treatment toward MOF precursor might improve the conductivity and charge

separation properties of the photocatalysts, so that the enhanced photocatalytic performances were accomplished.

Considering Inca marigold-flower-like MT-2 displayed highest photocatalytic Cr(VI) reduction efficiency, it was selected to conduct some subsequent experiments including the effects of pH values and co-existing ions. It has been found that pH exerted a significant influence on photocatalytic Cr(VI) reduction, in which the lower pH values were deemed to favor Cr(VI) reduction [51,52]. Generally, Cr(VI) existed in the form of Cr₂O₇²⁻ or HCrO₄⁻ under acidic condition, while the dominated species was CrO₄²⁻ in an alkaline environment [53,54]. The corresponding photocatalytic Cr(VI) reduction reaction over MT-2 can be proposed to follow Eqs. (3) and (4) in the presence of abundant H⁺, which was conducive to the conversion of Cr(VI) to Cr(III) [55,56]. As shown in Fig. 6d, the photocatalytic Cr(VI) reduction efficiency of MT-2 reached 100.0% within 60 min at pH = 2.0, which was superior to the efficiencies at pH being 4.0, 6.0 and 8.0. It worth noting that

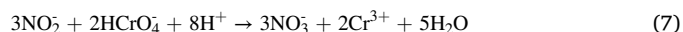
photocatalytic efficiency at pH = 8.0 decreased dramatically, which could be attributed to the mask of active sites by formed $\text{Cr}(\text{OH})_3$ precipitates (Eq. (5)) [23,57].



Previous studies reported that electron-hole pairs could be produced over the photocatalysts under the light irradiation. As well, photocatalytic Cr(VI) reduction performances would be enhanced after capturing photo-induced holes, because the recombination of electron-hole pairs can be suppressed [58–60]. Organic acids often exist in aquatic environments, which are considered as to be satisfying reducing agent. It has been reported that organic acids could act as hole scavengers [61] as well as reducing agent in photocatalysis [62]. In order to explore better conditions for photocatalytic activities, series organic matters including tartaric acid, citric acid and oxalic acid were selected to investigate their effects on Cr(VI) reduction, due to their difference in the number of α -hydroxyl carboxylate functional groups. As demonstrated in Fig. 7a and b, both the Cr(VI) reduction efficiencies and apparent rate constants (k) showed that the photocatalytic performances were obviously improved by adding tartaric acid (two α -hydroxyl groups), followed by citric acid (one α -hydroxyl group) and oxalic acid (no α -hydroxyl groups), which were consistent with the previous literatures [63,64].

Besides, the presence of foreign ions especially inorganic anions also exerted significant influence on photocatalytic activities [65,66]. Therefore, the effects of various anions like PO_4^{3-} , Cl^- , HCO_3^- , NO_3^- and SO_4^{2-} on Cr(VI) reduction were studied. As illustrated in Fig. 7c and d, all inorganic anions exhibited detrimental effects on the Cr(VI) reduction,

in which the k values followed the order of no anions (0.1059 min^{-1}) > NO_3^- (0.0274 min^{-1}) > HCO_3^- (0.0271 min^{-1}) > Cl^- (0.0234 min^{-1}) > SO_4^{2-} (0.0188 min^{-1}) > PO_4^{3-} (0.0094 min^{-1}). It was observed that both PO_4^{3-} and SO_4^{2-} displayed significant inhibition toward photocatalytic Cr(VI) reduction, and the corresponding efficiencies were decreased to 74.6% and 90.0%, respectively. It could be ascribed to the competitive adsorption between these anions, which made it difficult to capture Cr(VI) ions and resulted in the remarkable decrease of photocatalytic efficiency. In addition, the rate constant k for NO_3^- was higher than Cl^- , which was attributed to conversion of NO_3^- to NO_2^- , resulting in the positive effect on the photocatalytic reduction of Cr(VI) (Eqs. (6) and (7)) [67].



Since MT-2 exhibited considerable photocatalytic performances in the presence of inorganic ions and organic matters, it might display high efficiencies in real water samples. In order to further explore the practical applicability of MT-2, the Cr(VI) solutions simulated from real tap water and lake water (the concentrations of the common cations and anions in the real water samples can be found in Table S2) were treated with photocatalytic process. As shown in Fig. 8a, the photocatalytic Cr(VI) reduction efficiencies over MT-2 achieved 74.0% and 91.6% within 60 min, which was lower than the Cr(VI) solution simulated from deionized water. Also, the constant rate constant k also declined from 0.1059 min^{-1} to 0.0346 min^{-1} in lake water and 0.0243 min^{-1} in tap water, respectively, which could be attributed to the influence of foreign inorganic ions [68]. It worth noting that photocatalytic efficiency in lake water was more superior than that in tap water, due to the existence of organic matters that could facilitate charge carriers separation [69].

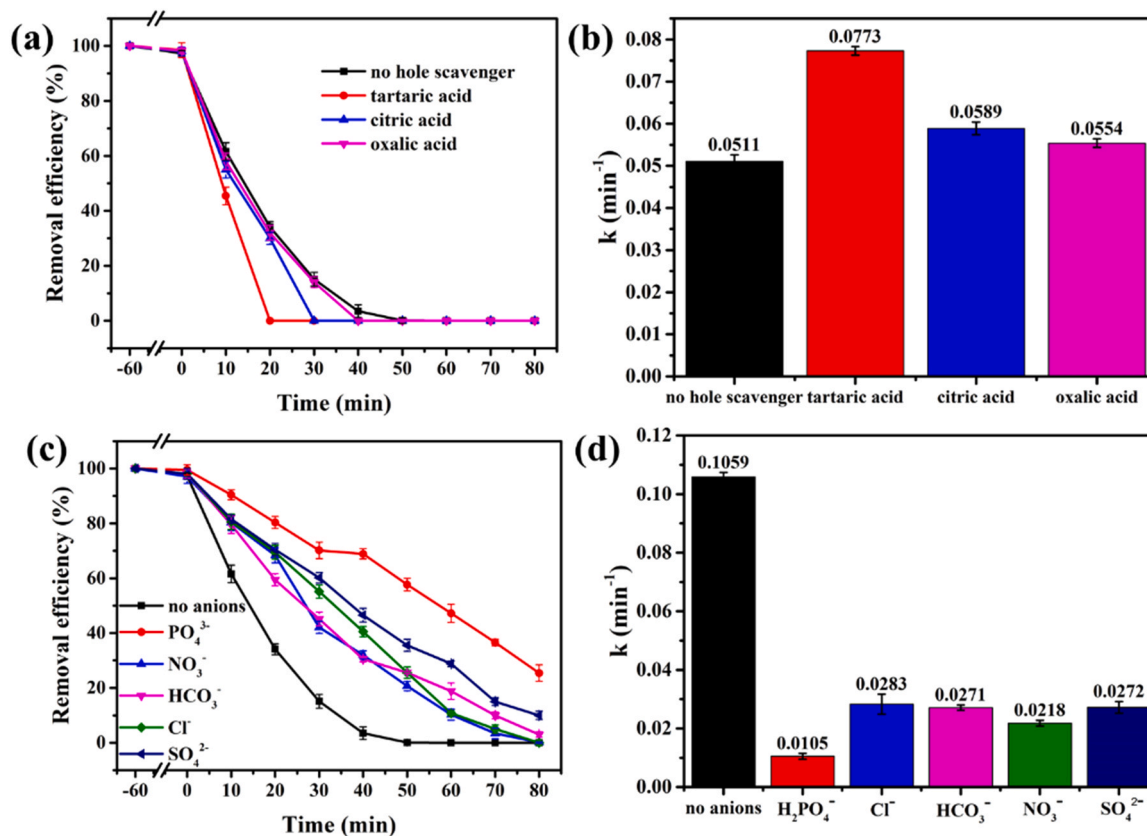


Fig. 7. Effect of different hole scavengers on Cr(VI) reduction efficiencies (a) and the corresponding rate constants (k) (b). Effect of inorganic anions toward Cr(VI) reduction efficiencies (c) and the corresponding rate constants (k) (d).

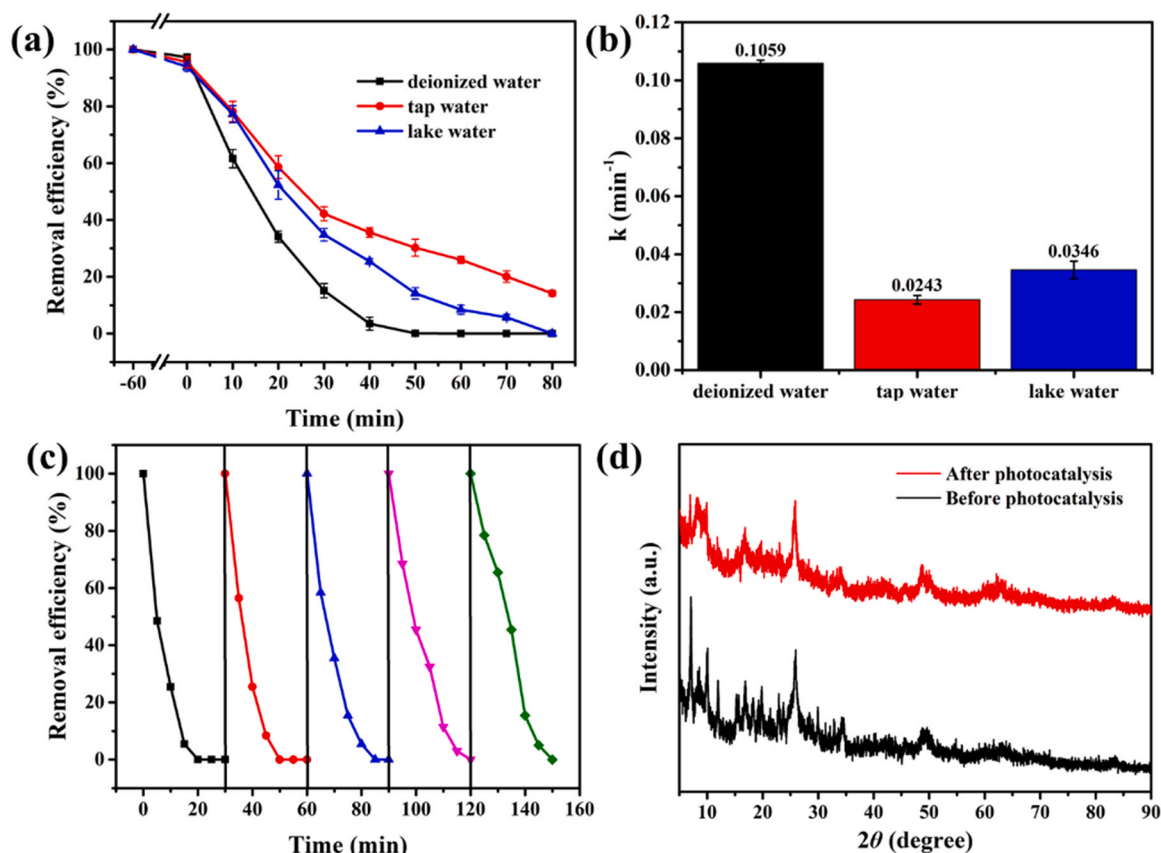


Fig. 8. The Cr(VI) photoreduction efficiencies (a) and rate constants k (b) in simulated wastewater prepared by different water. The cyclic experiments of photocatalytic Cr(VI) reaction by adding tartaric acid as hole scavenger (c). The PXRD patterns of MT-2 before and after Cr(VI) reduction experiments (d).

3.3. Reusability and stability of MT-2

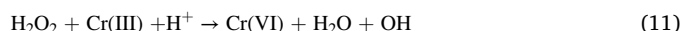
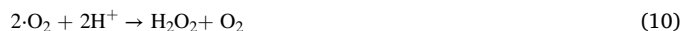
The reusability and stability of photocatalysts were essential properties for practical application. In this study, the long-term recyclability of MT-2 in photocatalytic Cr(VI) reduction was investigated. As depicted in Fig. 8a, the photocatalytic efficiencies still reach 100.0% after five cycles in the presence of tartaric acid as hole scavengers as well as photochemical reducing agent. Moreover, it could be observed from the PXRD patterns (Fig. 8d) and FTIR spectra (Fig. S7) of MT-2 before and after photocatalysis that both the chemical constitution and crystalline structure of MT-2 maintained well. Furthermore, the SEM and TEM images (Fig. S8) showed that the morphology experienced no noticeable changes, indicating that the MIL-125 core could be well protected by the external TiO₂ shell in the Inca marigold-flower-like MT-2.

3.4. Photocatalytic Cr(VI) reduction mechanism

Generally, the arc radius in Nyquist impedance plots represented charge transfer resistance (R_{ct}). It was reported that arcs with smaller radius possessed lower charge transfer resistance [70]. As shown in Fig. 9a, the arc radius followed the order of MT-2 < MT-1 < MT-3 < MT-6 < MIL-125, which corresponded well to the photocatalytic Cr(VI) reduction performances over the above-stated catalysts. It was implied that the MT-2, i.e. Inca marigold-flower-like TiO₂/MIL-125 composite presented most effective separation of photo-induced electron-hole pairs.

The determination of active species is important to explore the photocatalytic mechanism. Series active species capture agents including K₂S₂O₈, isopropyl alcohol (IPA) and EDTA-2Na were introduced to quench e⁻, ·OH and h⁺ [71–74]. As depicted in Fig. 9b, photocatalytic efficiencies decreased to 75.0% within 80 min when K₂S₂O₈

was added. It has been reported that ·O₂ was beneficial to Cr(VI) reduction [75]. Therefore, the Cr(VI) reduction experiment was conducted in the N₂ gas ambient to remove the dissolved oxygen (DO). The results showed that the rate of photocatalytic Cr(VI) reduction declined from 0.0511 min⁻¹ to 0.0269 min⁻¹ within 30 min, indicating that ·O₂ might participate in the photocatalytic reaction. In the presence of IPA, the corresponding Cr(VI) reduction efficiency decreased by 8.7%, which could be explained by Eqs. (8), (10) and (11). Furthermore, the efficiency and rate of Cr(VI) reduction was enhanced after adding EDTA-2Na, which could quench h⁺ to suppress the recombination of charge carriers.



In addition, Mott-Schottky measurements were carried out to determine the position of the conduction band (CB) and charge transfer. As shown in Fig. 9c and d, it can be observed that slope of C^2 value versus potential was positive, indicating MIL-125 precursor and MT-6 (TiO₂ derivative) were both n-type semiconductors. The calculated CB of MIL-125 precursor and MT-6 (TiO₂ derivative) were ca. -1.50 eV and -0.50 eV versus the Ag/AgCl electrode at pH = 7.0, corresponding to the reported literature [76,77]. Therefore, the obtained valence bands (VB) of MIL-125 and MT-6 were 2.10 eV and 2.88 eV vs. NHE according to Eq. (12) [78].

$$E_{\text{CB}} = E_{\text{VB}} - E_g \quad (12)$$

Based on the above results, the possible type-II heterojunction

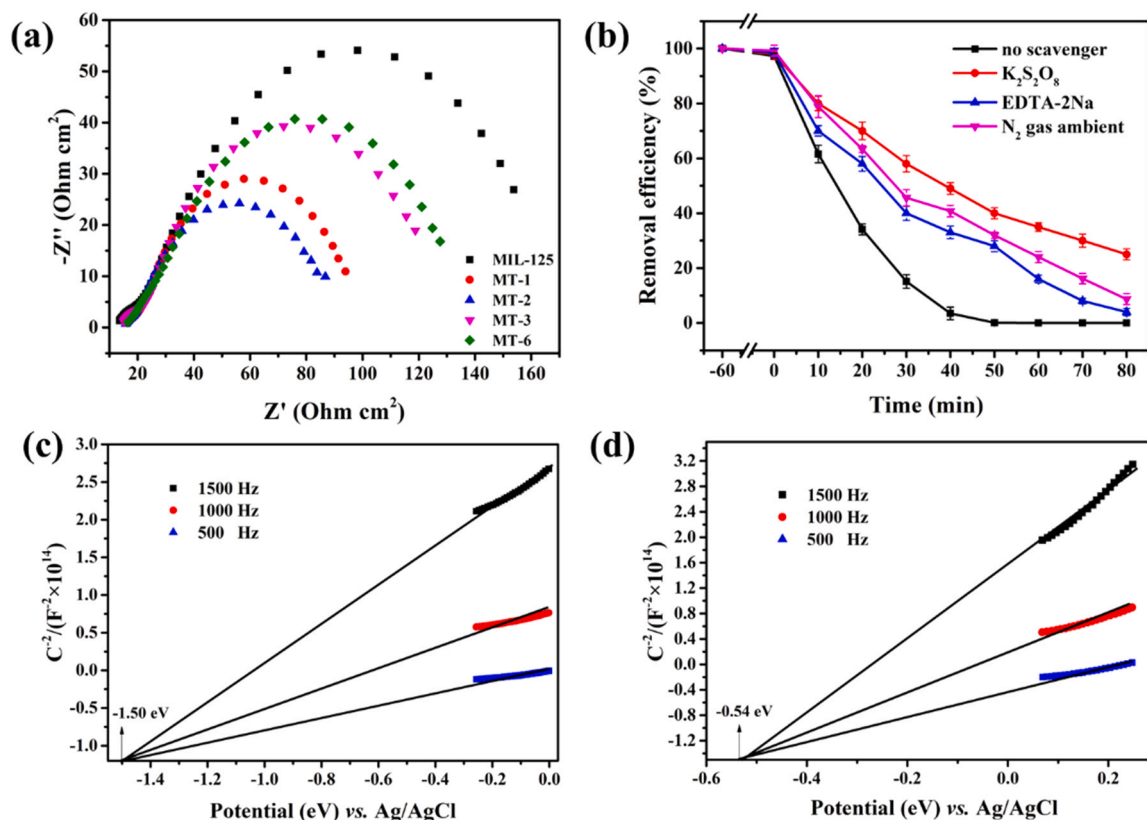


Fig. 9. The Electrochemical impedance spectra over MIL-125 and MT-x (a). Effect of different scavengers on Cr(VI) reduction (b). Mott-Schottky curves of MIL-125 (c) and MT-6 (anatase TiO₂) (d) at different frequencies.

mechanism of photocatalytic Cr(VI) reduction over MT-2 was speculated. Previous reports demonstrated that the metal ions or clusters and organic linkers in MOFs can absorb light and then achieve ligand-to-metal charge transfer (LMCT) or metal-to-ligand charge transfer (MLCT) due to their semiconducting properties [79]. As shown in Fig. 10, both MIL-125 precursor and MT-6 (TiO₂ products) could be excited to produce electrons and holes under the light irradiation. The photo-induced electrons on the LUMO of pristine MIL-125 could be transferred to the CB of TiO₂ due to the potential difference, which inhibited the recombination of photo-induced electron-hole pairs. Specifically, unsaturated Ti-O cluster in MT-2 would also contribute to charge transfer from MIL-125 core to TiO₂ shell. It can be observed that the potential of O₂/·O₂⁻ (-0.33 eV vs. NHE) was positive than that of

TiO₂ [75,80]. Furthermore, the ESR measurement also shown that the DMPO-·O₂⁻ signals of MT-2 were observed for 5 min and 10 min, while no signals were detected in dark (Fig. S9), confirming ·O₂⁻ could be produced.

To further verified the speculation, photo-deposition of Pt nanoparticles was carried out to ascertain the charge transfer route [81]. It was believed that electrons could be accepted by H₂PtCl₆ to form Pt⁰ nanoparticles, which would be deposited around the electron-rich sites [82]. As shown in Fig. 11, spherical nanoparticles were observed around the external shell of MT-2 (TiO₂/MIL-125) after photo-deposition. EDS element content analysis demonstrated that the spherical particles were composed of Pt. The lattice fringes of 0.227 nm corresponded to the (111) plane of Pt⁰ nanoparticle [83]. The photo-deposition experiment could provide a solid evidence to confirm the II-scheme mechanism.

4. Conclusions

In summary, we adopted a facile post-solvothermal method to prepare novel marigold-flower-like TiO₂/MIL-125 with MIL-125 as a precursor, which displayed better photocatalytic Cr(VI) performances compared to its precursor, the derived TiO₂ and even other heterostructures constructed by MIL-125. The AQE values demonstrated the photocatalytic process. Additionally, different influence factors on photocatalytic activities including pH values, foreign ions and organic acid were investigated. The positions of CB and LUMO were measured by Mott-Schottky curve. Combined with photo-deposition experiment, II-scheme mechanism for photoreduction of Cr(VI) was speculated. The cycle experiments demonstrated that MT-2 possessed good reusability and stability. This work confirms the emerging approach for fabricating photocatalysts derived from MOFs and opens up a new pathway for water remediation.

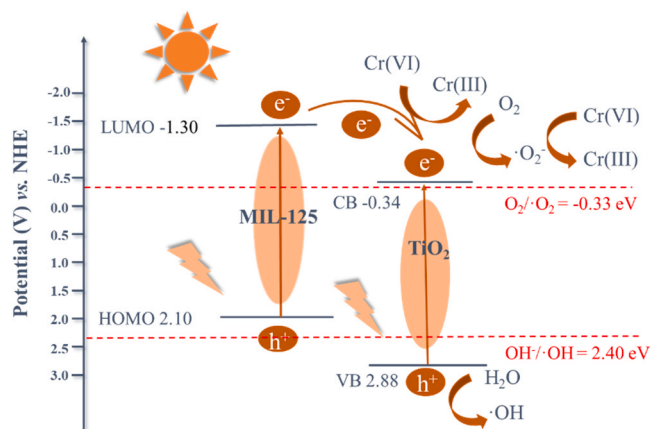


Fig. 10. Illustration of plausible mechanism of photocatalysis reduction of Cr(VI).

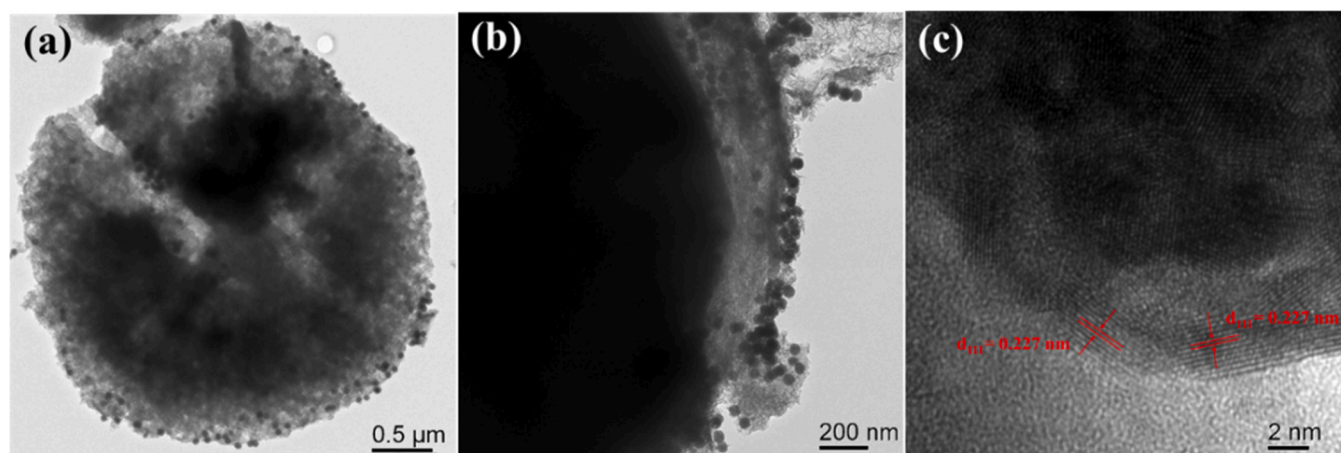


Fig. 11. The TEM images (a) (b) and HRTEM image (c) of MT-2 after photo-deposition of Pt nanoparticles.

CRediT authorship contribution statement

Yu-Xuan Li: Data curation, Investigation, Visualization, Writing - original draft preparation. **Chong-Chen Wang:** Conceptualization, Funding acquisition, Supervision, Project administration, Writing - review & editing. **Huifen Fu:** Methodology, Validation, Software. **Peng Wang:** Resources, Instrument.

Declaration of Competing Interest

The authors declare that they have no known competing financial interests or personal relationships that could have appeared to influence the work reported in this paper.

Acknowledgments

This work was supported by National Natural Science Foundation of China (51878023), Beijing Natural Science Foundation (8202016), Great Wall Scholars Training Program Project of Beijing Municipality Universities (CIT&TCD20180323), Beijing Talent Project (2020A27) and The Fundamental Research Funds for Beijing University of Civil Engineering and Architecture (X20147/X20141/X20135/X20146).

Appendix A. Supporting information

Supplementary data associated with this article can be found in the online version at doi:10.1016/j.jece.2021.105451.

References

- J. Schneider, M. Matsuoka, M. Takeuchi, J. Zhang, Y. Horiuchi, M. Anpo, D. W. Bahnemann, Understanding TiO₂ photocatalysis: mechanisms and materials, *Chem. Rev.* 114 (2014) 9919–9986.
- D. Wang, M. Wang, Z. Li, Fe-based metal-organic frameworks for highly selective photocatalytic benzene hydroxylation to phenol, *ACS Catal.* 5 (2015) 6852–6857.
- Y. Fu, D. Sun, Y. Chen, R. Huang, Z. Ding, X. Fu, Z. Li, An amine-functionalized titanium metal-organic framework photocatalyst with visible-light-induced activity for CO₂ reduction, *Angew. Chem. Int. Ed.* 51 (2012) 3364–3367.
- S. Zhao, Y. Wang, J. Dong, C.-T. He, H. Yin, P. An, K. Zhao, X. Zhang, C. Gao, L. Zhang, J. Lv, J. Wang, J. Zhang, A.M. Khattak, N.A. Khan, Z. Wei, J. Zhang, S. Liu, H. Zhao, Z. Tang, Ultrathin metal-organic framework nanosheets for electrocatalytic oxygen evolution, *Nat. Energy* 1 (2016) 16184.
- G. Huang, Q. Yang, Q. Xu, S.H. Yu, H.L. Jiang, Polydimethylsiloxane coating for a palladium/MOF composite: highly improved catalytic performance by surface hydrophobization, *Angew. Chem.* 128 (2016) 7505–7509.
- X. Yuan, H. Wang, Y. Wu, G. Zeng, X. Chen, L. Leng, Z. Wu, H. Li, One-pot self-assembly and photoreduction synthesis of silver nanoparticle-decorated reduced graphene oxide/MIL-125(Ti) photocatalyst with improved visible light photocatalytic activity, *Appl. Organomet. Chem.* 30 (2016) 289–296.
- Y.-X. Li, H. Fu, P. Wang, C. Zhao, W. Liu, C.-C. Wang, Porous tube-like ZnS derived from rod-like ZIF-L for photocatalytic Cr(VI) reduction and organic pollutants degradation, *Environ. Pollut.* 256 (2020), 113417.
- E. Dhivya, D. Magadevan, Y. Palguna, T. Mishra, N. Aman, Synthesis of titanium based hetero MOF photocatalyst for reduction of Cr(VI) from wastewater, *J. Environ. Chem. Eng.* 7 (2019), 103240.
- Z. Wang, X. Xu, J. Kim, V. Malgras, R. Mo, C. Li, Y. Lin, H. Tan, J. Tang, L. Pan, Y. Bando, T. Yang, Y. Yamauchi, Nanoarchitected metal-organic framework/polypyrrole hybrids for brackish water desalination using capacitive deionization, *Mater. Horiz.* 6 (2019) 1433–1437.
- X. Xu, T. Yang, Q. Zhang, W. Xia, Z. Ding, K. Eid, A.M. Abdullah, M. Shahriar, A. Hossain, S. Zhang, J. Tang, L. Pan, Y. Yamauchi, Ultrahigh capacitive deionization performance by 3D interconnected MOF-derived nitrogen-doped carbon tubes, *Chem. Eng. J.* 390 (2020), 124493.
- H. Wang, X. Yuan, Y. Wu, G. Zeng, H. Dong, X. Chen, L. Leng, Z. Wu, L. Peng, In situ synthesis of In₂S₃@MIL-125(Ti) core-shell microparticle for the removal of tetracycline from wastewater by integrated adsorption and visible-light-driven photocatalysis, *Appl. Catal. B: Environ.* 186 (2016) 19–29.
- Z. Yang, X. Xu, X. Liang, C. Lei, Y. Cui, W. Wu, Y. Yang, Z. Zhang, Z. Lei, Construction of heterostructured MIL-125/Ag/g-C₃N₄ nanocomposite as an efficient bifunctional visible light photocatalyst for the organic oxidation and reduction reactions, *Appl. Catal. B: Environ.* 205 (2017) 42–54.
- C. Zhao, Z. Wang, X. Chen, H. Chu, H. Fu, C.-C. Wang, Robust photocatalytic benzene degradation using mesoporous disk-like N-TiO₂ derived from MIL-125(Ti), *Chin. J. Catal.* 41 (2020) 1186–1197.
- J. Chen, X. Zhang, F. Bi, X. Zhang, Y. Yang, Y. Wang, A facile synthesis for uniform tablet-like TiO₂/C derived from Materials of Institut Lavoisier-125(Ti) (MIL-125 (Ti)) and their enhanced visible light-driven photodegradation of tetracycline, *J. Colloid Interface Sci.* 571 (2020) 275–284.
- L. Wu, H. Fu, Q. Wei, Q. Zhao, P. Wang, C.-C. Wang, Porous Cd_{0.5}Zn_{0.5}S nanocages derived from ZIF-8: boosted photocatalytic performances under LED-visible light, *Environ. Sci. Pollut. Res.* (2020).
- Y.-X. Li, Y.-C. Han, C.-C. Wang, Fabrication strategies and Cr(VI) elimination activities of the MOF-derivatives and their composites, *Chem. Eng. J.* 405 (2021), 126648.
- K.-Y. Zou, Z.-X. Li, Controllable syntheses of MOF-derived materials, *Chem. – A Eur. J.* 24 (2018) 6506–6518.
- Q. Hou, X. Li, Y. Pi, J. Xiao, Construction of In₂S₃@NH₂-MIL-68(In)/In₂S₃ sandwich homologous heterojunction for efficient CO₂ photoreduction, *Ind. Eng. Chem. Res.* 59 (2020) 20711–20718.
- B. Zhang, J. Zhang, X. Tan, D. Shao, J. Shi, L. Zheng, J. Zhang, G. Yang, B. Han, MIL-125-NH₂@TiO₂ core-shell particles produced by a post-solvothermal route for high-performance photocatalytic H₂ production, *ACS Appl. Mater. Interfaces* 10 (2018) 16418–16423.
- J. Geng, F. Gu, J. Chang, Fabrication of magnetic lignosulfonate using ultrasonic-assisted in situ synthesis for efficient removal of Cr(VI) and Rhodamine B from wastewater, *J. Hazard. Mater.* 375 (2019) 174–181.
- X. Wang, Y.-X. Li, X.-H. Yi, C. Zhao, P. Wang, J. Deng, C.-C. Wang, Photocatalytic Cr(VI) elimination over BUC-21/N-K₂Ti₄O₉ composites: Big differences in performance resulting from small differences in composition, *Chin. J. Catal.* 42 (2021) 259–270.
- S. Hou, X. Xu, M. Wang, T. Lu, C.Q. Sun, L. Pan, Synergistic conversion and removal of total Cr from aqueous solution by photocatalysis and capacitive deionization, *Chem. Eng. J.* 337 (2018) 398–404.
- H. Wang, X. Yuan, Y. Wu, G. Zeng, X. Chen, L. Leng, Z. Wu, L. Jiang, H. Li, Facile synthesis of amino-functionalized titanium metal-organic frameworks and their superior visible-light photocatalytic activity for Cr(VI) reduction, *J. Hazard. Mater.* 286 (2015) 187–194.
- Y.-C. Zhou, P. Wang, H. Fu, C. Zhao, C.-C. Wang, Ternary Ag/Ag₃PO₄/MIL-125-NH₂ Z-scheme heterojunction for boosted photocatalytic Cr(VI) cleanup under visible light, *Chin. Chem. Lett.* 31 (2020) 2645–2650.
- J.-W. Wang, F.-G. Qiu, P. Wang, C. Ge, C.-C. Wang, Boosted bisphenol A and Cr(VI) cleanup over Z-scheme WO₃/MIL-100(Fe) composites under visible light, *J. Clean. Prod.* 279 (2021), 123408.

- [26] C.-L. Hsu, S.-L. Wang, Y.-M. Tzou, Photocatalytic reduction of Cr(VI) in the presence of NO_3^- and Cl^- electrolytes as influenced by Fe(III), *Environ. Sci. Technol.* 41 (2007) 7907–7914.
- [27] Y.-X. Li, X. Wang, C.-C. Wang, H. Fu, Y. Liu, P. Wang, C. Zhao, S-TiO₂/UiO-66-NH₂ composite for boosted photocatalytic Cr(VI) reduction and bisphenol A degradation under LED visible light, *J. Hazard. Mater.* 399 (2020), 123085.
- [28] J. Sabate, M.A. Anderson, M.A. Aguado, J. Giménez, S. Cervera-March, C.G. Hill, Comparison of TiO₂ powder suspensions and TiO₂ ceramic membranes supported on glass as photocatalytic systems in the reduction of chromium(VI), *J. Mol. Catal.* 71 (1992) 57–68.
- [29] N.D. McNamara, G.T. Neumann, E.T. Masko, J.A. Urban, J.C. Hicks, Catalytic performance and stability of (V) MIL-47 and (Ti) MIL-125 in the oxidative desulfurization of heterocyclic aromatic sulfur compounds, *J. Catal.* 305 (2013) 217–226.
- [30] Y. Ren, J. Zhang, Y. Liu, H. Li, H. Wei, B. Li, X. Wang, Synthesis and superior anode performances of TiO₂-Carbon-rGO composites in lithium-ion batteries, *ACS Appl. Mater. Interfaces* 4 (2012) 4776–4780.
- [31] S. Wanjale, M. Birajdar, J. Jog, R. Neppalli, V. Causin, J. Karger-Kocsis, J. Lee, P. Panzade, Surface tailored PS/TiO₂ composite nanofiber membrane for copper removal from water, *J. Colloid Interface Sci.* 469 (2016) 31–37.
- [32] A. Mishra, A. Mehta, M. Sharma, S. Basu, Impact of Ag nanoparticles on photomineralization of chlorobenzene by TiO₂/bentonite nanocomposite, *J. Environ. Chem. Eng.* 5 (2017) 644–651.
- [33] H. Guo, F. Lin, J. Chen, F. Li, W. Wang, Metal-organic framework MIL-125(Ti) for efficient adsorptive removal of Rhodamine B from aqueous solution, *Appl. Organomet. Chem.* 29 (2015) 12–19.
- [34] R. Bibi, H. Huang, M. Kalulu, Q. Shen, L. Wei, O. Oderinde, N. Li, J. Zhou, Synthesis of amino-functionalized Ti-MOF derived yolk-shell and hollow heterostructures for enhanced photocatalytic hydrogen production under visible light, *ACS Sustain. Chem. Eng.* 7 (2019) 4868–4877.
- [35] H. Fu, X. Wang, P. Wang, Z. Wang, H. Ren, C.-C. Wang, Enhanced acetone sensing performance of Au nanoparticle modified porous tube-like ZnO derived from rod-like ZIF-L, *Dalton Trans.* 47 (2018) 9014–9020.
- [36] X. Yang, Z. Wen, Z. Wu, X. Luo, Synthesis of ZnO/ZIF-8 hybrid photocatalysts derived from ZIF-8 with enhanced photocatalytic activity, *Inorg. Chem. Front.* 5 (2018) 687–693.
- [37] Y. Wang, Y. Huang, W. Ho, L. Zhang, Z. Zou, S. Lee, Biomolecule-controlled hydrothermal synthesis of C–N–S-tridoped TiO₂ nanocrystalline photocatalysts for NO removal under simulated solar light irradiation, *J. Hazard. Mater.* 169 (2009) 77–87.
- [38] H.B. Wu, H.H. Hng, X.W. Lou, Direct synthesis of anatase TiO₂ nanowires with enhanced photocatalytic activity, *Adv. Mater.* 24 (2012) 2567–2571.
- [39] V. Subramanian, A. Karki, K.I. Gnanasekar, F.P. Eddy, B. Rambabu, Nanocrystalline TiO₂ (anatase) for Li-ion batteries, *J. Power Sources* 159 (2006) 186–192.
- [40] X. Jiang, Y. Zhang, J. Jiang, Y. Rong, Y. Wang, Y. Wu, C. Pan, Characterization of oxygen vacancy associates within hydrogenated TiO₂: A positron annihilation study, *J. Phys. Chem. C* 116 (2012) 22619–22624.
- [41] Y. Zhuang, L. Sun, S. Zeng, W. Zhan, X.-J. Wang, Y. Zhao, X. Han, Engineering migration pathway for effective separation of photogenerated carriers on multicomponent heterojunctions coated with nitrogen-doped carbon, *Chem. – A Eur. J.* 25 (2019) 14133–14139.
- [42] K. Gao, Y. Li, P. Na, Insight into design of MIL-125(Ti)-based composite with boosting photocatalytic activity: the embedded multiple Fe oxide count, *Adv. Mater. Interfaces* 7 (2020), 1901449.
- [43] J. Qiu, L. Yang, M. Li, J. Yao, Metal nanoparticles decorated MIL-125-NH₂ and MIL-125 for efficient photocatalysis, *Mater. Res. Bull.* 112 (2019) 297–306.
- [44] H. Wang, X. Yuan, Y. Wu, X. Chen, L. Leng, G. Zeng, Photodeposition of metal sulfides on titanium metal-organic frameworks for excellent visible-light-driven photocatalytic Cr(VI) reduction, *RSC Adv.* 5 (2015) 32531–32535.
- [45] M. Wang, L. Yang, J. Yuan, L. He, Y. Song, H. Zhang, Z. Zhang, S. Fang, Heterostructured Bi₂S₃@NH₂-MIL-125 (Ti) nanocomposite as a bifunctional photocatalyst for Cr (vi) reduction and rhodamine B degradation under visible light, *RSC Adv.* 8 (2018) 12459–12470.
- [46] K. Gao, J. Chen, Z. Liu, Y. Li, Y. Wu, J. Zhao, P. Na, Intensified redox co-conversion of As(III) and Cr(VI) with MIL-125(Ti)-derived COOH functionalized TiO₂: Performance and mechanism, *Chem. Eng. J.* 360 (2019) 1223–1232.
- [47] C.J. Murphy, J.M. Buriak, Best practices for the reporting of colloidal inorganic nanomaterials, *Chem. Mater.* 27 (2015) 4911–4913.
- [48] Y. Zhang, S.-J. Park, Stabilization of dispersed CuPd bimetallic alloy nanoparticles on ZIF-8 for photoreduction of Cr(VI) in aqueous solution, *Chem. Eng. J.* 369 (2019) 353–362.
- [49] D.S. Kim, S.-Y. Kwak, The hydrothermal synthesis of mesoporous TiO₂ with high crystallinity, thermal stability, large surface area, and enhanced photocatalytic activity, *Appl. Catal. A: Gen.* 323 (2007) 110–118.
- [50] X.L. Wang, H.G. Yang, Facile fabrication of high-yield graphitic carbon nitride with a large surface area using bifunctional urea for enhanced photocatalytic performance, *Appl. Catal. B: Environ.* 205 (2017) 624–630.
- [51] Y. Ku, I.-L. Jung, Photocatalytic reduction of Cr(VI) in aqueous solutions by UV irradiation with the presence of titanium dioxide, *Water Res.* 35 (2001) 135–142.
- [52] A. Idris, N. Hassan, N.S. Mohd Ismail, E. Misran, N.M. Yusof, A.-F. Ngomsik, A. Bee, Photocatalytic magnetic separable beads for chromium(VI) reduction, *Water Res.* 44 (2010) 1683–1688.
- [53] C.E. Barrera-Díaz, V. Lugo-Lugo, B. Bilyeu, A review of chemical, electrochemical and biological methods for aqueous Cr(VI) reduction, *J. Hazard. Mater.* 223–224 (2012) 1–12.
- [54] J. Guo, J.-J. Li, C.-C. Wang, Adsorptive removal of Cr(VI) from simulated wastewater in MOF BUC-17 ultrafine powder, *J. Environ. Chem. Eng.* 7 (2019), 102909.
- [55] L. Shi, T. Wang, H. Zhang, K. Chang, X. Meng, H. Liu, J. Ye, An amine-functionalized iron(III) metal-organic framework as efficient visible-light photocatalyst for Cr(VI) reduction, *Adv. Sci.* 2 (2015), 1500006.
- [56] Z. Ren, X. Liu, H. Chu, H. Yu, Y. Xu, W. Zheng, W. Lei, P. Chen, J. Li, C. Li, Carbon quantum dots decorated MoSe₂ photocatalyst for Cr(VI) reduction in the UV–vis–NIR photon energy range, *J. Colloid Interface Sci.* 488 (2017) 190–195.
- [57] F. Zhang, Y. Zhang, G. Zhang, Z. Yang, D.D. Dionysiou, A. Zhu, Exceptional synergistic enhancement of the photocatalytic activity of SnS₂ by coupling with polyaniline and N-doped reduced graphene oxide, *Appl. Catal. B: Environ.* 236 (2018) 53–63.
- [58] A.E. Giannakas, M. Antonopoulou, Y. Deligiannakis, I. Konstantinou, Preparation, characterization of N–I co-doped TiO₂ and catalytic performance toward simultaneous Cr(VI) reduction and benzoic acid oxidation, *Appl. Catal. B: Environ.* 140–141 (2013) 636–645.
- [59] X.-H. Yi, S.-Q. Ma, X.-D. Du, C. Zhao, H. Fu, P. Wang, C.-C. Wang, The facile fabrication of 2D/3D Z-scheme g-C₃N₄/UiO-66 heterojunction with enhanced photocatalytic Cr(VI) reduction performance under white light, *Chem. Eng. J.* 375 (2019), 121944.
- [60] R. Qiu, D. Zhang, Z. Diao, X. Huang, C. He, J.-L. Morel, Y. Xiong, Visible light induced photocatalytic reduction of Cr(VI) over polymer-sensitized TiO₂ and its synergism with phenol oxidation, *Water Res.* 46 (2012) 2299–2306.
- [61] T. Tan, D. Beydoun, R. Amal, Effects of organic hole scavengers on the photocatalytic reduction of selenium anions, *J. Photochem. Photobiol. A: Chem.* 159 (2003) 273–280.
- [62] J.J. Testa, M.A. Grela, M.I. Litter, Heterogeneous photocatalytic reduction of chromium(VI) over TiO₂ particles in the presence of oxalate: involvement of Cr(V) species, *Environ. Sci. Technol.* 38 (2004) 1589–1594.
- [63] M. Rivero-Huguet, W.D. Marshall, Influence of various organic molecules on the reduction of hexavalent chromium mediated by zero-valent iron, *Chemosphere* 76 (2009) 1240–1248.
- [64] X.H. Yi, F.X. Wang, X.D. Du, P. Wang, C.-C. Wang, Enhanced photocatalytic Cr(VI) reduction over BUC-21/g-C₃N₄ composites under simulated sunlight irradiation, *Appl. Organomet. Chem.* 33 (2019), e4621.
- [65] U.I. Gaya, A.H. Abdullah, Z. Zainal, M.Z. Hussein, Photocatalytic treatment of 4-chlorophenol in aqueous ZnO suspensions: intermediates, influence of dosage and inorganic anions, *J. Hazard. Mater.* 168 (2009) 57–63.
- [66] C. Zhao, J. Wang, X. Chen, Z. Wang, H. Ji, L. Chen, W. Liu, C.-C. Wang, Bifunctional Bi₁₂O₁₇Cl₂/MIL-100(Fe) composites toward photocatalytic Cr(VI) sequestration and activation of persulfate for bisphenol A degradation, *Sci. Total Environ.* 752 (2021), 141901.
- [67] Y.-M. Tzou, C.-L. Hsu, C.-C. Chen, J.-H. Chen, J.-J. Wu, K.-J. Tseng, Influence of inorganic anion on Cr(VI) photo-reduction in the presence of ferric ion, *J. Hazard. Mater.* 156 (2008) 374–380.
- [68] X. Wei, P. Wang, H. Fu, C. Zhao, C.-C. Wang, Boosted photocatalytic elimination toward Cr(VI) and organic pollutants over BUC-21/Cd_{0.5}Zn_{0.5}S under LED visible light, *Mater. Res. Bull.* 129 (2020), 110903.
- [69] L. Li, Z. Xu, F. Liu, Y. Shao, J. Wang, H. Wan, S. Zheng, Photocatalytic nitrate reduction over Pt-Cu/TiO₂ catalysts with benzene as hole scavenger, *J. Photochem. Photobiol. A: Chem.* 212 (2010) 113–121.
- [70] Y. Liu, C. Zeng, L. Ai, J. Jiang, Boosting charge transfer and hydrogen evolution performance of CdS nanocrystals hybridized with MoS₂ nanosheets under visible light irradiation, *Appl. Surf. Sci.* 484 (2019) 692–700.
- [71] X. Tong, X. Cao, T. Han, W.-C. Cheong, R. Lin, Z. Chen, D. Wang, C. Chen, Q. Peng, Y. Li, Convenient fabrication of BiOBr ultrathin nanosheets with rich oxygen vacancies for photocatalytic selective oxidation of secondary amines, *Nano Res.* 12 (2019) 1625–1630.
- [72] X. Qiao, C. Wang, Y. Niu, N-Benzyl HMTA induced self-assembly of organic-inorganic hybrid materials for efficient photocatalytic degradation of tetracycline, *J. Hazard. Mater.* 391 (2020), 122121.
- [73] J. Li, X. Zhang, F. Raziq, J. Wang, C. Liu, Y. Liu, J. Sun, R. Yan, B. Qu, C. Qin, L. Jing, Improved photocatalytic activities of g-C₃N₄ nanosheets by effectively trapping holes with halogen-induced surface polarization and 2,4-dichlorophenol decomposition mechanism, *Appl. Catal. B: Environ.* 218 (2017) 60–67.
- [74] L. Peng, Y. Bian, X. Shen, H.-C. Yao, H. Chen, Z. Li, Efficient silver nanocluster photocatalyst for simultaneous methyl orange/4-chlorophenol oxidation and Cr (VI) reduction, *Chin. Chem. Lett.* 31 (2020) 2871–2875.
- [75] X. Hu, H. Ji, F. Chang, Y. Luo, Simultaneous photocatalytic Cr(VI) reduction and 2,4,6-TCP oxidation over g-C₃N₄ under visible light irradiation, *Catal. Today* 224 (2014) 34–40.
- [76] N. Li, X. Liu, J. Zhou, W. Chen, M. Liu, Encapsulating CuO quantum dots in MIL-125(Ti) coupled with g-C₃N₄ for efficient photocatalytic CO₂ reduction, *Chem. Eng. J.* 399 (2020), 125782.
- [77] Y. Zhao, X. Huang, X. Tan, T. Yu, X. Li, L. Yang, S. Wang, Fabrication of BiOBr nanosheets@TiO₂ nanobelts p–n junction photocatalysts for enhanced visible-light activity, *Appl. Surf. Sci.* 365 (2016) 209–217.
- [78] Y. Gong, X. Zhao, H. Zhang, B. Yang, K. Xiao, T. Guo, J. Zhang, H. Shao, Y. Wang, G. Yu, MOF-derived nitrogen doped carbon modified g-C₃N₄ heterostructure composite with enhanced photocatalytic activity for bisphenol A degradation with peroxymonosulfate under visible light irradiation, *Appl. Catal. B: Environ.* 233 (2018) 35–45.
- [79] Y. Fang, Y. Ma, M. Zheng, P. Yang, A.M. Asiri, X. Wang, Metal-organic frameworks for solar energy conversion by photoredox catalysis, *Coord. Chem. Rev.* 373 (2018) 83–115.

- [80] C. Zhao, Z. Wang, X. Li, X. Yi, H. Chu, X. Chen, C.-C. Wang, Facile fabrication of BUC-21/Bi₂₄O₃₁Br₁₀ composites for enhanced photocatalytic Cr(VI) reduction under white light, *Chem. Eng. J.* 389 (2020), 123431.
- [81] R. Cao, H. Yang, S. Zhang, X. Xu, Engineering of Z-scheme 2D/3D architectures with Ni(OH)₂ on 3D porous g-C₃N₄ for efficiently photocatalytic H₂ evolution, *Appl. Catal. B: Environ.* 258 (2019), 117997.
- [82] W. Jiang, X. Zong, L. An, S. Hua, X. Miao, S. Luan, Y. Wen, F.F. Tao, Z. Sun, Consciously constructing heterojunction or direct Z-scheme photocatalysts by regulating electron flow direction, *ACS Catal.* 8 (2018) 2209–2217.
- [83] Y. Li, W. Gao, L. Ci, C. Wang, P.M. Ajayan, Catalytic performance of Pt nanoparticles on reduced graphene oxide for methanol electro-oxidation, *Carbon* 48 (2010) 1124–1130.